

# SCIENTIFIC REPORTS



OPEN

## Resolution-enhanced Fourier ptychographic microscopy based on high-numerical-aperture illuminations

Jiasong Sun<sup>1,2</sup>, Chao Zuo<sup>1,2</sup>, Liang Zhang<sup>1,2</sup> & Qian Chen<sup>2</sup>

High-resolution and wide field-of-view (FOV) microscopic imaging plays a central role in diverse applications such as high-throughput screening and digital pathology. However, conventional microscopes face inherent trade-offs between the spatial resolution and FOV, which are fundamental limited by the space-bandwidth product (SBP) of the optical system. The resolution-FOV tradeoff can be effectively decoupled in Fourier ptychography microscopy (FPM), however, to date, the effective imaging NA achievable with a typical FPM system is still limited to the range of 0.4–0.7. Herein, we report, for the first time, a high-NA illumination based resolution-enhanced FPM (REFPM) platform, in which a LED-array-based digital oil-immersion condenser is used to create high-angle programmable plane-wave illuminations, endowing a 10×, 0.4 NA objective lens with final effective imaging performance of 1.6 NA. With REFPM, we present the highest-resolution results with a unprecedented half-pitch resolution of 154 nm at a wavelength of 435 nm across a wide FOV of 2.34 mm<sup>2</sup>, corresponding to an SBP of 98.5 megapixels (~50 times higher than that of the conventional incoherent microscope with the same resolution). Our work provides an important step of FPM towards high-resolution large-NA imaging applications, generating comparable resolution performance but significantly broadening the FOV of conventional oil-immersion microscopes.

High-resolution wide-field imaging is essential for various applications in different fields, such as biological, biomedical research and digital pathology, which require large space-bandwidth product (SBP) to provide computational and statistical analyses for thousands of cells simultaneously across a wide field-of-view (FOV)<sup>1–4</sup>. However, conventional microscopes are always beset by the inherent trade-offs between the spatial resolution and FOV, limiting their SBPs and application areas. In the last decades, an enormous amount of research and considerable effort has been devoted to creating high-resolution wide-field microscopy techniques, like mechanical scanning and stitching, synthetic aperture microscopy, lens-free on-chip super-resolution technique, and Fourier ptychography microscopy (FPM)<sup>5–13</sup>. FPM is a recently developed technique that overcomes the physical SBP limit of a bright-field microscope by transforming the challenge into which can be solved through computation<sup>13,14</sup>. Instead of starting with high resolution and stitching together a larger FOV, FPM uses low NA objective lens to take advantage of its innate large FOV and stitches together images in Fourier space to recover high resolution. Illumination angles are scanned sequentially with a programmable light-emitting diode (LED) array, shifting different amounts of high spatial frequency information into the low NA objective lens. This resolution improvement is analogous to coherent aperture synthesis<sup>8,9,15–18</sup> and structured-illumination<sup>5,6,19–22</sup> imaging. But distinct from synthetic aperture, FPM uses nonlinear optimization algorithms<sup>13,23–25</sup> similar to translational diversity<sup>26,27</sup> and ptychography<sup>28–31</sup> to perform the reconstruction instead. Since the FOV is fixed in FPM and the final reconstruction resolution is determined by the sum of the objective lens and illumination NAs, the ratio of  $NA_{ill}$  (illumination NA) to  $NA_{obj}$  (objective NA) becomes the dominant factor for achieving higher improvement of SBP. To

<sup>1</sup>Smart Computational Imaging (SCI) Laboratory, Nanjing University of Science and Technology, Nanjing, Jiangsu Province, 210094, China. <sup>2</sup>Jiangsu Key Laboratory of Spectral Imaging & Intelligent Sense, Nanjing University of Science and Technology, Nanjing, Jiangsu Province, 210094, China. Correspondence and requests for materials should be addressed to C.Z. (email: [zuochoa@njust.edu.cn](mailto:zuochoa@njust.edu.cn)) or Q.C. (email: [chenqian@njust.edu.cn](mailto:chenqian@njust.edu.cn))

be more precisely, the theoretical enhancement of SBP just equals  $\left(1 + \frac{NA_{ill}}{NA_{obj}}\right)^2$ , explaining why most FPM platforms employ low NA objective lens with high illumination angles.

Although many significant progresses have been made in FPM for achieving higher data acquisition efficiency<sup>24, 32–34</sup> and recovery accuracy<sup>23, 34–39</sup> in the past few years, little is pursuing a larger SBP with high synthetic NA ( $NA_{syn}$ ) greater than unity. Since the illumination brightness, the angle of divergence for each LED element, and the flexibility of the commercial LED board are all limited by the processing technology, the illumination angles in most FPM systems have been limited to an NA of less than about 0.3–0.6. Thus the highest achievable half-pitch resolution for those reported FPM setups is usually constrained between 500–700 nm, which is far away from the need of recent high-resolution-imaging applications. In order to further improve the recovery resolution, instead of enlarging  $NA_{ill}$ , a high-numerical-aperture FPM is implemented using high magnification objective lenses with large  $NA_{obj}$  to achieve the final  $NA_{syn}$  of 1.45<sup>36</sup>. However, since the reduction of FOV is much larger than the improvement of resolution in this FPM platform, the SBP is suppressed to some extent, making this FPM technique less appealing.

Herein, we introduce a resolution-enhanced FPM setup, termed REFPM, which utilizes an LED array and an oil-immersion condenser to significantly improve the recovery resolution of conventional FPM with an expanded  $NA_{ill}$  greater than unity, without sacrificing the FOV. In REFPM platform, the oil-immersion condenser collects the illumination lights from every LED elements and transfers them into plane-waves, achieving a striking  $NA_{ill}$  of 0.93 (dry) and 1.2 (oil). Although it seems convenient to directly expand the  $NA_{ill}$  by using an oil-immersion condenser, additional challenges have been brought about for achieving higher resolution accurately. Aiming to satisfy the sampling criteria for FPM in object and frequency space, we employ a denser LED array and carefully design our REFPM setup with proper system parameters, pushing the limit of resolving power of FPM while keeping the imaging field of view (FOV) uncompromised. Furthermore, in order to compensate the imperfections and uncertainties of the optical system, a series of computational correction methods are implemented in our iterative reconstruction algorithm. We evaluate the importance of each correction method experimentally and overcome those physical limitations and problems, such as pixel aliasing problem, illumination brightness inhomogeneity, and LED positional misalignment through computational correction. Finally, using 261 different illumination angles with a  $10\times/0.4NA$  objective lens, we achieved an effective  $NA_{syn}$  of  $\sim 1.6$  and a half-pitch resolution of 154 nm at a wavelength of 435 nm across a large FOV of 2.34 mm<sup>2</sup>, which constitutes a SBP of 98.7 megapixels. We also compare the performance of our REFPM setup against other commonly available high-NA microscopes, including conventional oil-immersion microscopes. The reconstructed results indicate that REFPM achieves a large SBP nearly 50 times higher than that of the conventional incoherent microscope with the same resolution. Therefore, this unique technique could not only generate comparable resolution performance but also significantly broaden the FOV of conventional oil-immersion microscopes, which would provide an important step of FPM towards high-resolution large-NA imaging applications.

## Results

**Resolution and SBP of different microscopy systems.** We evaluate the performance of the REFPM platform by reconstructing a resolution target. Figure 1 compares the resolution and SBP of conventional bright-field microscopy and REFPM systems for the same USAF resolution target. Figure 1(a) shows the full FOV of the incoherent microscopy image using a  $10\times/0.4NA$  objective lens with 0.4 NA green light illumination. The windowed small region in Fig. 1(a) is enlarged and presented in Fig. 1(b2), while the same part of the microscopy image in red and blue channels are presented in Fig. 1(b1,b3). As can be seen, the highest distinguishable resolution target elements in Fig. 1(b1–b3) are Elements 5 in Group 9, limited by the imaging pixel-size  $\left(\frac{6.5\mu m}{10} = 650\text{ nm}\right)$ . We further enlarge the middle part of the resolution target to present patterns in Group 10 and Group 11 more clearly [Fig. 1(c1–c3)]. Since the imaging resolution is limited by the camera, all the patterns in Fig. 1(c1–c3) cannot be recognized. We also performed a set of simulations to validate how does this imaging pixel-size restrict the resolution (Supplementary Information A). Next, using a  $60\times/1.35NA$  objective lens with 1.2 NA monochromatic illuminations, high-resolution incoherent microscopy results are obtained, as shown in Fig. 1(d1–d3). The line-scan profiles from the selected positions in Fig. 1(d1–d3) are given in top three rows of Fig. 1(g). By employing REFPM with a  $10\times/0.4NA$  objective lens and 0.93 NA monochromatic illuminations, intensity recovery results are obtained, as shown in Fig. 1(e1–e3). Here, we used the oil-immersion condenser but did not add the immersion oil between the sample and the condenser. Thus, the  $NA_{ill}$  could not surpass 1 in this condition. Comparing the theoretical (237 nm, 197 nm, 164 nm) and measured half-pitch resolutions (218 nm, 194 nm, 173 nm) in three channels, it indicates that this REFPM system could nearly achieve the theoretical  $NA_{syn}$  of 1.33 (dry). Next, we added the immersion oil between the target and the condenser for raising the  $NA_{ill}$  to 1.2. As can be seen in Fig. 1(f1–f3), comparing the theoretical (197 nm, 164 nm, 136 nm) and measured half-pitch resolutions (194 nm, 173 nm, 154 nm) in three channels, a  $NA_{syn}$  close to 1.6 (oil) is realized using this REFPM system. Table 1 summarizes the SBPs which are achieved using these four microscopy systems, and it is obvious that our REFPM platform is able to provide an SBP about 98.5 megapixels, which is nearly 50 times higher than that of the conventional bright-field microscope with the same resolution. In Supplementary Video 1, we show a zooming video of the full-FOV raw image captured with conventional incoherent microscope ( $NA_{obj} = 0.4$ ,  $NA_{ill} = 0.4$ ,  $\lambda = 435\text{ nm}$ ) and the reconstructed full-FOV image using REFPM ( $NA_{obj} = 0.4$ ,  $NA_{ill} = 1.2$ ,  $\lambda = 435\text{ nm}$ ).

**Effectiveness of the correction methods.** To validate the effectiveness of those correction methods described below, Fig. 2 shows some enlarged sub-regions from the recovered images using different FPM reconstruction methods. All the reconstruction results are recovered from the same raw low-resolution images when



**Figure 1.** Imaging and recovery results of conventional bright-field microscopy and REFPM systems for the same USAF resolution target. **(a)** The full FOV of the incoherent microscopy image using a  $10 \times 0.4$  NA objective lens with 0.4 NA illumination. **(b,c)** Enlarged sub-regions of Fig. 1(a) in R/G/B channels. **(d)** High-resolution incoherent microscopy results using a  $60 \times 1.35$  NA objective lens with 1.2 NA illumination in three channels. **(e,f)** REFPM recovery results obtained by employing a  $10 \times 0.4$  NA objective lens with 0.93 NA and 1.2 NA illumination in R/G/B channels. **(g)** Line-scan profiles from the selected position of targets in Fig. 1(d1–f3).

Half-pitch resolution and SBP for microscopy systems ( $\lambda = 435 \text{ nm}$ )								
	Objective lens	FOV ( $\text{mm}^2$ )	Illumination NA	Theoretical synthetic NA	Theoretical half-pitch resolution (nm)	Theoretical SBP (megapixels)	Measured half-pitch resolution (nm)	Measured SBP (megapixels)
Conventional incoherent microscopy	$10 \times 0.40 \text{ NA}$	2.34	0.40 NA	0.80 NA	332	21.2	615	6.19
	$60 \times 1.35 \text{ NA}$	0.06	1.20 NA	2.55 NA	104	6	173	2.17
REFPM	$10 \times 0.40 \text{ NA}$	2.34	0.93 NA	1.33 NA	164	87	173	78.2
	$10 \times 0.40 \text{ NA}$	2.34	1.20 NA	1.60 NA	136	125	154	98.7

**Table 1.** Comparison of the measured half-pitch resolution, FOV, and SBP that are achieved using four different microscopy systems.

having the same iterative times. The REFPM with all the correction methods provides the best reconstruction quality and its recovered intensity images in R/G/B three channels are illustrated in Fig. 2(a1–a3). Next, if we do not calibrate the illumination brightness before iterations, the resolution targets are deformed a bit, and a lot of mesh patterns will emerge in the background noticeably, as shown in Fig. 2(b1–b3). Then, by implementing the REFPM without adaptive step-size strategy, the edge of the resolution elements is distorted and the highest achievable resolutions in the R/G/B three channels decreased a little [Fig. 2(c1–c3)]. According to the sampling criterion for FPM in object space, when we use the red light to illuminate the object, Nyquist criterion is satisfied in the imaging system of our REFPM platform. But those low-resolution images in blue channel are suffering from serious pixel aliasing problem. Therefore, we got the same results in the red channel with [Fig. 2(a1)] or without [Fig. 2(d1)] using the upsampling strategy. But in the blue channel, reconstruction quality reduced significantly without the help of upsampling strategy [Fig. 2(d3)]. At last, as introduced in ref. 37, the recovery quality is very sensitive to the positional misalignment of the LED array. Thus, once we remove the LED position correction process from the REFPM algorithm, the reconstructed results would be extremely distorted and nearly none of the resolution elements in Group 11 is distinguishable [Fig. 2(e1–e3)]. Therefore, the significance of these correction methods has been illustrated clearly by comparing reconstruction results in Fig. 2. It indicates that the LED positional misalignment correction process is the pivotal point for not only achieving this unprecedented high resolution with low-NA objective lens, but relaxing the requirement of optical aligning. Moreover, if the Nyquist criterion is not satisfied and pixel aliasing problem occurs, the upsampled FPM method with sufficient data redundancy could still guarantee the recovery accuracy.

**Wide-FOV high-resolution microscopy of stained cell sample.** To obtain color images of the stained human blood cells via REFPM, we repeat the capture and reconstruction steps three separate times using red, green and blue LED illuminations from the same LED array, and then place each reconstruction in the appropriate color channel for the final color image in Fig. 3. We detail imaging performance in a selected image sub-regions, marked by black squares in Fig. 3(a). Images from the conventional color microscope setup, using the same  $10\times$  and  $60\times$  objective lenses as noted above, are shown in Fig. 3(b1,c1). Image clarity increases as the objective lens NA increases, but at a sacrifice of a smaller FOV (marked with blue dashed window in Fig. 3(a)). The same sub-regions from our  $1.33 NA_{syn}$  and  $1.6 NA_{syn}$  REFPM reconstructions are presented in Fig. 3(d1,e1). The REFPM recovered image with  $1.6 NA_{syn}$  contains details that are not resolved in any of the other images. For example, a stained blood cell from Fig. 3(e1) is further zoomed in (Fig. 3(e2)), showing two-point structure (pointed by blue arrows) that are clearly resolved by  $1.6 NA$  REFPM (Fig. 3(e3)). In comparison, for  $60\times$  oil-immersion microscope and the  $1.33 NA$  REFPM, this two-point structure is vaguely resolved (Fig. 3(c3,d3)), while REFPM provides a better imaging quality with higher contrast ratio. Furthermore, the recovered phase distribution of this blood cell smear is illustrated in Fig. 4(a). This phase map is recovered with  $1.6 NA_{syn}$  in the red channel and it is displayed in false color. The enlarged sub-regions of Fig. 4(a) are shown in Fig. 4(b,c) to illustrate the phase recovery quality of our REFPM system. In addition, our method also applies to unstained cells and a set of recovered phase maps can be found in Supplementary Information B.

## Discussion

In this paper, we report a high-NA illumination based resolution-enhanced FPM platform, named REFPM, to generate high-resolution large-SBP reconstructions from a series of low-resolution raw images with the help of a  $1.2 NA$  oil-immersion condenser and a  $0.4 NA$  objective lens. It is demonstrated that REFPM system can significantly improve the resolution and achieve the final effective imaging performance of  $1.6 NA$ , corresponding to a half-pitch resolution of  $154 \text{ nm}$  with a FOV of  $2.34 \text{ mm}^2$  at a wavelength of  $435 \text{ nm}$ . The maximum achievable SBP of our microscope is about  $98.5$  megapixels, which is nearly  $50$  times higher than that of the conventional incoherent microscope with the same resolution. We also investigate the importance of a series of correction algorithms for overcoming the physical limitations and uncertainties of the optical system, such as illumination brightness inhomogeneity, imaging noise, LED positional misalignment, and pixel aliasing problem. Those high-quality reconstructed results demonstrate that REFPM not only extends the SBP of conventional microscopes, but also yields a significantly enhanced imaging resolution far beyond (up to 3–4 times) the coherent diffraction limit, which makes it highly appealing for those applications that require high-resolution and large-SBP at the same time.



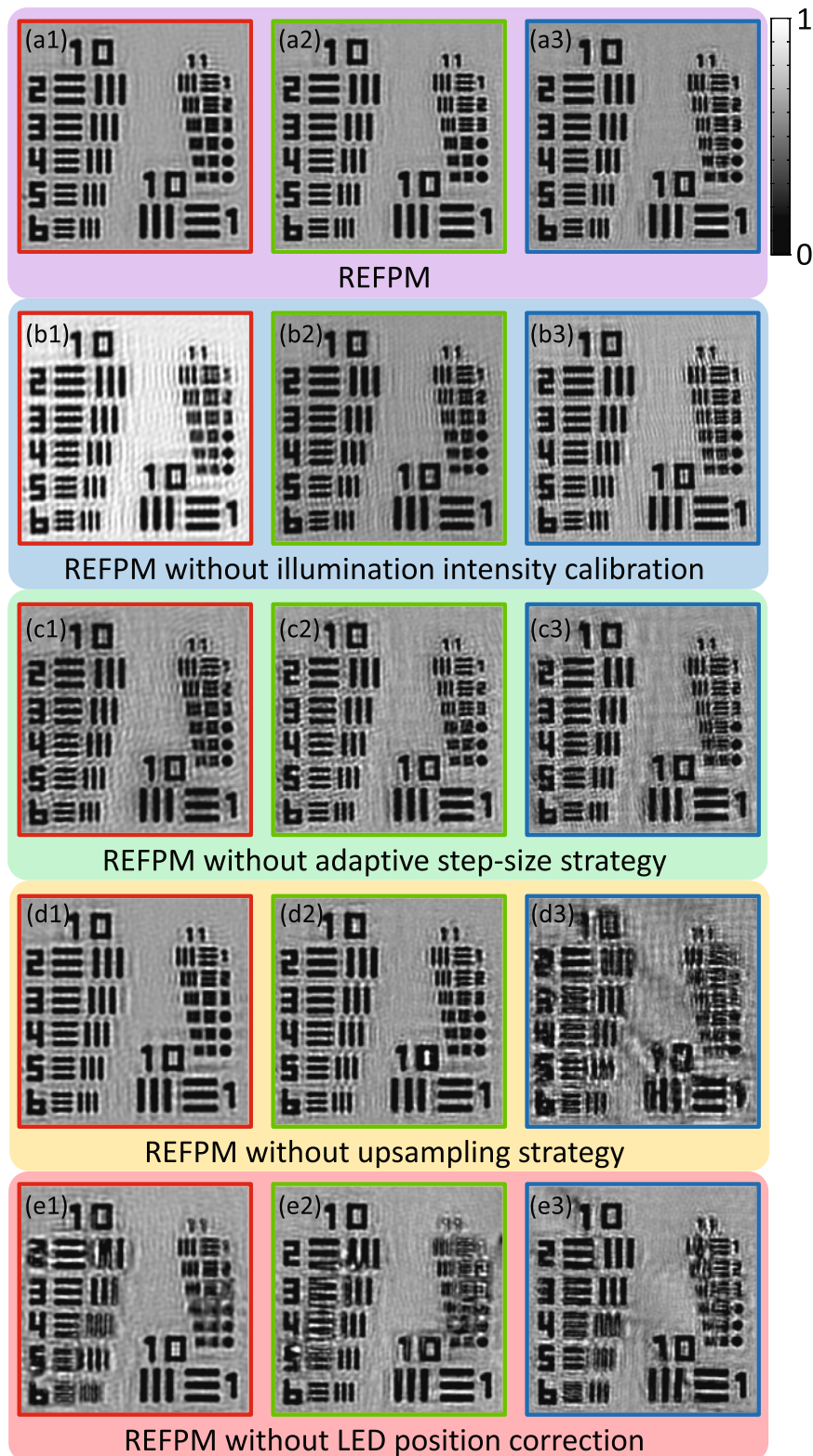


**Figure 2.** Comparison of the enlarged sub-regions of the measured USAF resolution target using different FPM reconstruction methods. (a) Reconstructed intensity images in R/G/B channels using REFPM with all the correction methods implemented in this work. (b–e) REFPM recovered results in three channels without using illumination brightness calibration, adaptive step-size strategy, upsampling strategy, or positional misalignment correction respectively.

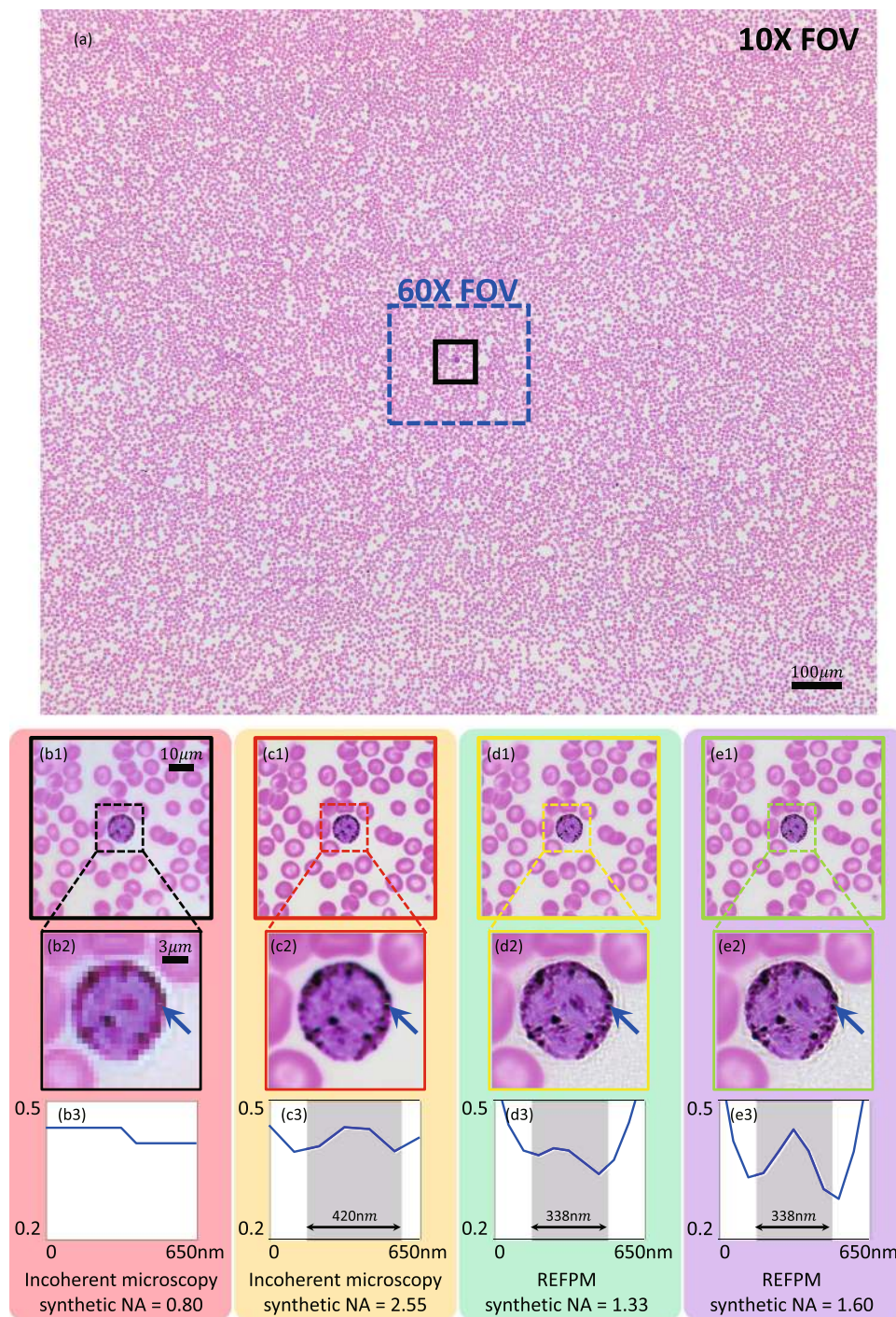


**Figure 3.** Imaging and recovery results of conventional bright-field microscopy and REFPM systems for the same human blood cell smear. **(a)** The full FOV of the incoherent microscopy image using a  $10 \times 0.4$  NA objective lens with  $0.4$  NA illumination. **(b1)** Enlarged sub-regions of Fig. 3(a). **(c1–e1)** Imaging and recovery results of the same sub-region using conventional bright-field microscopy and REFPM with different  $NA_{syn}$ . **(b2–e2)** Color images of a stained blood cell using four different microscopy methods. **(b3–e3)** Line-scan profiles of the two-point structure from the position pointed by arrows in Fig. 3(b2–e2).

## Materials and Methods

**Optical setup.** As depicted in Fig. 5, the REFPM setup in this paper consists of three major components: a programmable LED array, an oil-immersion condenser, and a microscopic imaging system. The commercial, multi-wavelength surface-mounted LED array (1.667 mm spacing) is placed at the front focal plane of the condenser to illuminate the specimen from different angles. The central wavelengths in R/G/B channels are 632 nm, 525 nm, 435 nm respectively, and the spectral linewidth at each wavelength is  $\sim 20$  nm. During the imaging process, 261 LED elements on the board are lighted up sequentially and all of them are driven statically using a



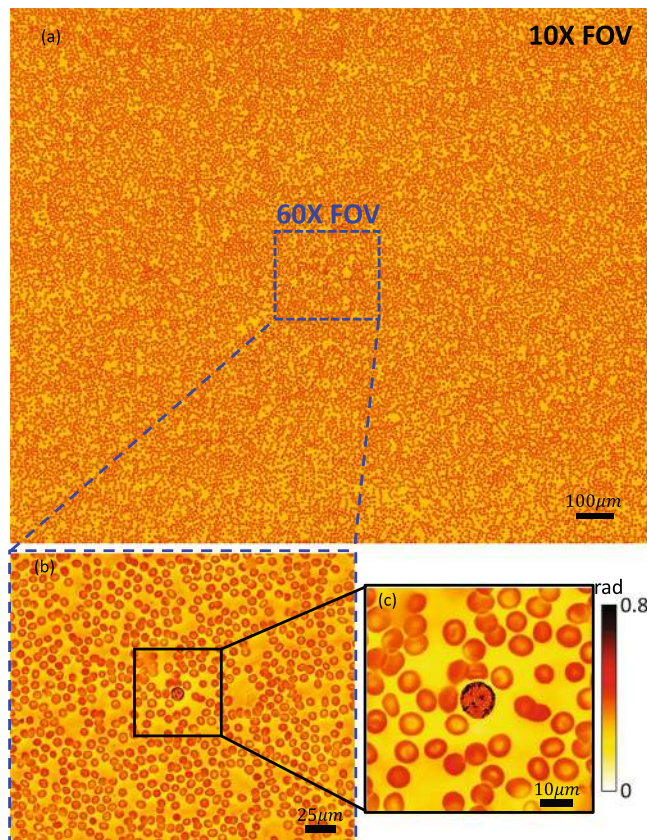


**Figure 4.** Recovered phase distribution of the blood cell smear using our REFPM platform. (a) The full FOV of the retrieved phase map using a  $10 \times 0.4$  NA objective lens with 1.2 NA illumination. (b,c) Enlarged sub-regions of Fig. 4(a).

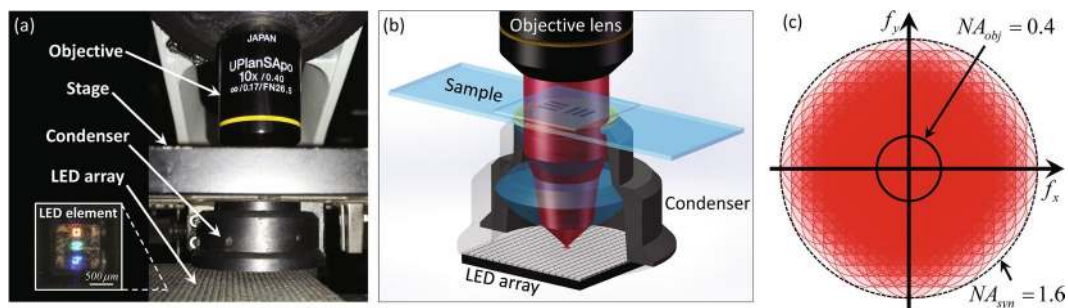


**Figure 5.** Optical setup of the LED array and condenser-based REFPM platform. (a) The experimental setup involves an LED array board, an oil-immersion condenser (1.20 NA) and an Olympus UPlanSApo  $10 \times (0.40$  NA) objective lens. (b) Schematic diagram of the illumination system in our REFPM platform. (c) Synthesized frequency apertures in the Fourier space using REFPM.

self-made LED controller board with an FPGA unit (EP4CE10E22C8N) to provide the logical control. The imaging system consists of two parts: a commercial bright-field microscope (CX22, Olympus, Japan) and a scientific CMOS camera (PCO.edge 5.5, 6.5  $\mu\text{m}$  pixel pitch). The camera is synchronized with the LED array by the same controller via two coaxial cables that provide the trigger and monitor the exposure status. We experimentally measure the system frame rate to be  $\sim 33$  Hz for capturing full-frame ( $2560 \times 2160$ ) 16-bit images. Thus, all those 261 images are captured within 8 seconds. The data are transferred to the computer via a CameraLink interface.

**Sample preparation.** The Extreme resolution target (Ready Optics Company, Calabasas, California, USA), 1951 USAF board from Group 4 to Group 11 (137 nm minimum spacing), is embedded in a standard microscope slide that suitable for oil-immersion objectives and oil-immersion condensers. The blood cell smear sample (Carolina Biological Supply Company, Burlington, North Carolina, USA) is prepared using normal (healthful)

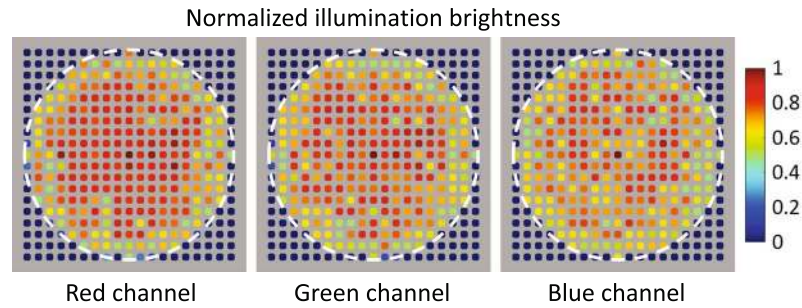


**Figure 6.** Normalized illumination brightness of every LED elements in R/G/B channels.

human blood and stained with hematoxylin and eosin<sup>40</sup> to show general framework of crimson and white blood cells.

**Illumination brightness calibration.** The illumination inconformity of the LED elements is one of the major systematic errors of FPM platforms. In this work, we implement the calibration procedure before measurement using an oil-immersion objective lens ( $60\times/1.35$  NA) with the oil-immersion condenser (1.20 NA), and fill the space between them with microscope oil ( $n_{oil} = 1.518$ ). Since the NA of this objective lens is larger than that of the condenser, illumination lights from all the incident angles can be collected by the objective lens and recorded as bright-field images. First, we turn on the central LED in R/G/B channels sequentially and capture three monochrome images ( $\mathbf{I}_{1R}, \mathbf{I}_{1G}, \mathbf{I}_{1B}$ ) with a same exposure time. Generally, the average intensity values of these monochrome images  $\mathbf{I}_{1R,1G,1B}$  are quite different due to the brightness inconformity of the central LED in R/G/B channels. In order to balance the color of the LED array, we adjust the exposure times for the central LED in three channels to make sure that  $\mathbf{I}_{1R,1G,1B}$  have the same average intensity value. Next, all the LED elements are lighted up sequentially and 261 images are captured in each channel, considering the average intensity of each image as the illumination brightness of each LED element. After obtaining the brightness of all the LEDs, we divide them by the brightness of the central LED to generate the normalized illumination brightness in three channels. These normalized parameters will be used as the intensity correction factors in the post-processing procedure. When a set of low-resolution images are captured, before iterative reconstruction, they need to be divided by their corresponding normalized illumination brightness to computationally compensate the illumination inconformity of the LED elements. Figure 6 displays the normalized illumination brightness of every LED elements in R/G/B channels. It is obvious that the illumination inconformity of the LED elements could be really huge ( $\sim 50\%$  maximum intensity difference), which need to be calibrated properly to achieve the expected recovery accuracy. Note that, those brightness values which are zeros denote that their corresponding LED elements are exceeding the NA of the condenser.

**Adaptive step-size strategy for FPM.** Since the low-level of irradiance produces individual measurements that are heavily affected by noise in those dark-field images, we adopt the adaptive step-size strategy as introduced in ref. 39 to improve the stability and robustness of the reconstruction towards noise yet retain the fast initial convergence speed. In order to retrieve the pupil function of the objective lens, we implement the adaptive step-size strategy and an incremental gradient method<sup>24</sup> with pupil function recovery procedure based on the following equations,

$$\Psi_i^k = \mathcal{F} \left\{ \sqrt{\frac{\mathbf{I}_i}{|\mathcal{F}^{-1}\{\mathbf{P}_i^k \mathbf{O}_i^k\}|^2}} \mathcal{F}^{-1}\{\mathbf{P}_i^k \mathbf{O}_i^k\} \right\} \quad (1)$$

$$\mathbf{O}_{i+1}^k = \mathbf{O}_i^k - \alpha^k \frac{|\mathbf{P}_i^k|}{|\mathbf{P}_i^k|_{max} (|\mathbf{P}_i^k|^2 + \gamma)} \mathbf{P}_i^{k*} (\Psi_i^k - \mathbf{P}_i^k \mathbf{O}_i^k) \quad (2)$$

$$\mathbf{P}_{i+1}^k = \mathbf{P}_i^k - \beta^k \frac{|\mathbf{O}_i^k|}{|\mathbf{O}_i^k|_{max} (|\mathbf{O}_i^k|^2 + \gamma)} \mathbf{O}_i^{k*} (\Psi_i^k - \mathbf{P}_i^k \mathbf{O}_i^k) \quad (3)$$

where  $\Psi_i^k$  is updated sub-spectrum.  $k$  denotes the iteration number and  $i$  is the updating image number in this iteration.  $\alpha^k$  and  $\beta^k$  are the step-size for objective function  $\mathbf{O}_i^k$  and pupil function  $\mathbf{P}_i^k$ .  $\mathcal{F}\{\cdot\}$  denotes the discrete Fourier transform while  $\mathcal{F}^{-1}\{\cdot\}$  is the inverse discrete Fourier transform.  $\gamma$  is a small constant (normally  $\gamma = 0.01$ ) to avoid divide-by-zero problem when  $|\mathbf{O}_i^k|^2$  or  $|\mathbf{P}_i^k|^2$  is too small. In REFPM, both  $\alpha^k$  and  $\beta^k$  are halved when no apparent reduction in the error metric is made by the iteration. Moreover, in order to achieve additional improvements of the recovery accuracy, we initial the step-size  $\alpha$  and  $\beta$  as  $\alpha^0 = 1$ ,  $\beta^0 = \frac{1}{\sqrt{N}} \approx \frac{1}{16}$ , where  $N$  is the total number of LEDs in the NA of condenser ( $N = 261$ ).



**Upsampling strategy for FPM.** Pixel aliasing problem usually appears in the lens-free on-chip microscopy systems<sup>10, 12, 41, 42</sup>, because the high NA and the large pixel-size of those systems cannot satisfy the Nyquist sampling criterion. Similarly, the pixel aliasing problem could also appear in the FPM platforms. As introduced in ref. 38, the spatial-sampling-ratio of FPM can be presented as  $R_{cam} = \frac{\lambda}{NA_{obj} 2\Delta x_{cam} Mag}$ . Considering our REFPM setup ( $NA_{obj} = 0.4$ ,  $Mag = 10$ ,  $\Delta x_{cam} = 6.5 \mu m$ ,  $\lambda = 633, 525, 435 \text{ nm}$  in R/G/B channels respectively), the pixel aliasing problem would occur in the blue channel ( $R_{cam} = 1.22, 1.01, 0.84$  in R/G/B channels respectively). Thus we adopt an upsampled FPM method to obtain the expected reconstruction resolution<sup>38</sup>. In the upsampled FPM, we assume that the actual pixel-size of the sensor is reduced by half to guarantee the Nyquist sampling criterion and those low-resolution images are captured when pixel binning is enabled ( $2 \times 2$  pixels are combined into one pixel). During the iterative updating procedure, pixel binning processes are complemented computationally to realistically simulate the pixel aliasing problem in the experimental REFPM platform. Since the upsampling strategy for FPM won't reduce the recovery accuracy even if the spatial sampling criterion is satisfied<sup>38</sup>, we adopt this upsampling strategy in red and green channels too.

**LED positional misalignment correction.** As shown in the Fig. 5(a), the R/G/B radiation-emitting semiconductors in one LED are separated with each other at hundreds of micrometers. This little positional uncertainty could significantly affect the recovery accuracy. Therefore, we implement the LED positional misalignment correction method based on simulated annealing and non-linear regression algorithms<sup>37</sup> for 15 iterations to adjust the positioning errors of all the LED elements. Since the LED array is fixed under the condenser tightly in our REFPM platform, the positional calibration process would be performed only once using the USAF resolution target. Afterwards, the high-resolution images of other samples, such as human blood cell smear, could be reconstructed precisely with no more extra positional correction procedure. Note that the upsampling strategy need to be used in the positional correction process to make sure the positions of the blue LED elements are adjusted accurately. However, the adaptive step-size strategy should not be used in this correction process because if the positional misalignment has not been corrected completely, the decrease of the updating step-size would interfere the positional correction accuracy and result in residual positioning errors. So, in the positional misalignment correction process, we adopt fixed updating step-size  $\alpha = 1$ ,  $\beta = \frac{1}{16}$ .

**Computation platform used for REFPM.** Our reconstructions are performed using MATLAB (Version R2015b, MathWorks, Natick, Massachusetts) on a laptop computer equipped with a 2.60 GHz central processing unit (Intel Core i5-3320M) and 8 GB of random-access memory. In the reconstruction, we divided each full-FOV raw image ( $2560 \times 2160$  pixels) into  $12 \times 10$  sub-regions ( $360 \times 360$  pixels each), with a 160-pixel overlap on each side of neighboring sub-regions. Each set of images was then processed by the algorithm described above to create a high-resolution reconstruction having both intensity and phase ( $3600 \times 3600$  pixels). Finally, all high-resolution reconstructions were combined using the alpha-blending stitching method<sup>13</sup> to create the full-FOV high-resolution reconstruction. For each  $360 \times 360$  pixels sub-region with an upsampling factor of 10, the processing time of our iterative recovery routine takes  $\sim 30$  s. The total processing time for the full FOV was nearly 1 h, which could be further reduced by investigating the use of GPU acceleration for our algorithm.

## References

- Popescu, G. *et al.* Optical imaging of cell mass and growth dynamics. *American Journal of Physiology-Cell Physiology* **295**, C538–C544, doi:10.1152/ajpcell.00121.2008 (2008).
- Cohen, A. R., Gomes, F. L., Roysam, B. & Cayouette, M. Computational prediction of neural progenitor cellfates. *Nature methods* **7**, 213–218, doi:10.1038/nmeth.1424 (2010).
- Rimon, N. & Schuldiner, M. Getting the whole picture: combining throughput with content in microscopy. *J Cell Sci* **124**, 3743–3751, doi:10.1242/jcs.087486 (2011).
- Mir, M. *et al.* Optical measurement of cycle-dependent cell growth. *Proceedings of the National Academy of Sciences* **108**, 13124–13129, doi:10.1073/pnas.1100506108 (2011).
- Gustafsson, M. G. Nonlinear structured-illumination microscopy: wide-field fluorescence imaging with theoretically unlimited resolution. *Proceedings of the National Academy of Sciences of the United States of America* **102**, 13081–13086, doi:10.1073/pnas.0406877102 (2005).
- Gustafsson, M. G. *et al.* Three-dimensional resolution doubling in wide-field fluorescence microscopy by structured illumination. *Biophysical journal* **94**, 4957–4970, doi:10.1529/biophysj.107.120345 (2008).
- Ma, B. *et al.* Use of autostitch for automatic stitching of microscope images. *Micron* **38**, 492–499, doi:10.1016/j.micron.2006.07.027 (2007).
- Hillman, T. R., Gutzler, T., Alexandrov, S. A. & Sampson, D. D. High-resolution, wide-field object reconstruction with synthetic aperture fourier holographic optical microscopy. *Optics express* **17**, 7873–7892, doi:10.1364/OE.17.007873 (2009).
- Gutzler, T., Hillman, T. R., Alexandrov, S. A. & Sampson, D. D. Coherent aperture-synthesis, wide-field, high-resolution holographic microscopy of biological tissue. *Optics letters* **35**, 1136–1138, doi:10.1364/OL.35.001136 (2010).
- Bishara, W., Su, T.-W., Coskun, A. F. & Ozcan, A. Lensfree on-chip microscopy over a wide field-of-view using pixel super-resolution. *Optics express* **18**, 11181–11191, doi:10.1364/OE.18.011181 (2010).
- Zheng, G., Lee, S. A., Antebi, Y., Elowitz, M. B. & Yang, C. The epetri dish, an on-chip cell imaging platform based on subpixel perspective sweeping microscopy (spsm). *Proceedings of the National Academy of Sciences* **108**, 16889–16894, doi:10.1073/pnas.1110681108 (2011).
- Greenbaum, A. *et al.* Wide-field computational imaging of pathology slides using lens-free on-chip microscopy. *Science translational medicine* **6**, 267ra175–267ra175, doi:10.1126/scitranslmed.3009850 (2014).
- Zheng, G., Horstmeyer, R. & Yang, C. Wide-field, high-resolution fourier ptychographic microscopy. *Nature photonics* **7**, 739–745, doi:10.1038/nphoton.2013.187 (2013).
- Ou, X., Horstmeyer, R., Yang, C. & Zheng, G. Quantitative phase imaging via fourier ptychographic microscopy. *Optics letters* **38**, 4845–4848, doi:10.1364/OL.38.004845 (2013).
- Alexandrov, S. A., Hillman, T. R., Gutzler, T. & Sampson, D. D. Synthetic aperture fourier holographic optical microscopy. *Physical review letters* **97**, 168102, doi:10.1103/PhysRevLett.97.168102 (2006).

16. Feng, P., Wen, X. & Lu, R. Long-working-distance synthetic aperture fresnel off-axis digital holography. *Optics express* **17**, 5473–5480, doi:[10.1364/OE.17.005473](https://doi.org/10.1364/OE.17.005473) (2009).
17. Lee, D. J. & Weiner, A. M. Optical phase imaging using a synthetic aperture phase retrieval technique. *Optics express* **22**, 9380–9394, doi:[10.1364/OE.22.009380](https://doi.org/10.1364/OE.22.009380) (2014).
18. Tippie, A. E., Kumar, A. & Fienup, J. R. High-resolution synthetic-aperture digital holography with digital phase and pupil correction. *Optics express* **19**, 12027–12038, doi:[10.1364/OE.19.012027](https://doi.org/10.1364/OE.19.012027) (2011).
19. Gustafsson, M. G. Surpassing the lateral resolution limit by a factor of two using structured illumination microscopy. *Journal of microscopy* **198**, 82–87, doi:[10.1046/j.1365-2818.2000.00710.x](https://doi.org/10.1046/j.1365-2818.2000.00710.x) (2000).
20. York, A. G. *et al.* Resolution doubling in live, multicellular organisms via multifocal structured illumination microscopy. *Nature methods* **9**, 749–754, doi:[10.1038/nmeth.2025](https://doi.org/10.1038/nmeth.2025) (2012).
21. Chowdhury, S. & Izatt, J. Structured illumination quantitative phase microscopy for enhanced resolution amplitude and phase imaging. *Biomedical optics express* **4**, 1795–1805, doi:[10.1364/BOE.4.001795](https://doi.org/10.1364/BOE.4.001795) (2013).
22. Wicker, K. & Heintzmann, R. Resolving a misconception about structured illumination. *Nature Photonics* **8**, 342–344, doi:[10.1038/nphoton.2014.88](https://doi.org/10.1038/nphoton.2014.88) (2014).
23. Ou, X., Zheng, G. & Yang, C. Embedded pupil function recovery for fourier ptychographic microscopy. *Optics express* **22**, 4960–4972, doi:[10.1364/OE.22.004960](https://doi.org/10.1364/OE.22.004960) (2014).
24. Tian, L., Li, X., Ramchandran, K. & Waller, L. Multiplexed coded illumination for fourier ptychography with an led array microscope. *Biomedical optics express* **5**, 2376–2389, doi:[10.1364/BOE.5.002376](https://doi.org/10.1364/BOE.5.002376) (2014).
25. Tian, L. & Waller, L. 3d intensity and phase imaging from light field measurements in an led array microscope. *Optica* **2**, 104–111 (2015).
26. Rodenburg, J. M. & Faulkner, H. M. A phase retrieval algorithm for shifting illumination. *Applied physics letters* **85**, 4795–4797, doi:[10.1063/1.1823034](https://doi.org/10.1063/1.1823034) (2004).
27. Guizar-Sicairos, M. & Fienup, J. R. Phase retrieval with transverse translation diversity: a nonlinear optimization approach. *Optics express* **16**, 7264–7278, doi:[10.1364/OE.16.007264](https://doi.org/10.1364/OE.16.007264) (2008).
28. Maiden, A. M. & Rodenburg, J. M. An improved ptychographical phase retrieval algorithm for diffractive imaging. *Ultramicroscopy* **109**, 1256–1262, doi:[10.1016/j.ultramic.2009.05.012](https://doi.org/10.1016/j.ultramic.2009.05.012) (2009).
29. Thibault, P., Dierolf, M., Bunk, O., Menzel, A. & Pfeiffer, F. Probe retrieval in ptychographic coherent diffractive imaging. *Ultramicroscopy* **109**, 338–343, doi:[10.1016/j.ultramic.2008.12.011](https://doi.org/10.1016/j.ultramic.2008.12.011) (2009).
30. Maiden, A. M., Humphry, M. J. & Rodenburg, J. Ptychographic transmission microscopy in three dimensions using a multi-slice approach. *JOSA A* **29**, 1606–1614, doi:[10.1364/JOSAA.29.001606](https://doi.org/10.1364/JOSAA.29.001606) (2012).
31. Thibault, P. & Menzel, A. Reconstructing state mixtures from diffraction measurements. *Nature* **494**, 68–71, doi:[10.1038/nature11806](https://doi.org/10.1038/nature11806) (2013).
32. Bian, L. *et al.* Content adaptive illumination for fourier ptychography. *Optics letters* **39**, 6648–6651, doi:[10.1364/OL.39.006648](https://doi.org/10.1364/OL.39.006648) (2014).
33. Dong, S., Shiradkar, R., Nanda, P. & Zheng, G. Spectral multiplexing and coherent-state decomposition in fourier ptychographic imaging. *Biomedical optics express* **5**, 1757–1767, doi:[10.1364/BOE.5.001757](https://doi.org/10.1364/BOE.5.001757) (2014).
34. Tian, L. *et al.* Computational illumination for high-speed *in vitro* fourier ptychographic microscopy. *Optica* **2**, 904–911, doi:[10.1364/OPTICA.2.000904](https://doi.org/10.1364/OPTICA.2.000904) (2015).
35. Bian, Z., Dong, S. & Zheng, G. Adaptive system correction for robust fourier ptychographic imaging. *Optics express* **21**, 32400–32410 (2013).
36. Ou, X., Horstmeyer, R., Zheng, G. & Yang, C. High numerical aperture fourier ptychography: principle, implementation and characterization. *Optics express* **23**, 3472–3491, doi:[10.1364/OE.23.003472](https://doi.org/10.1364/OE.23.003472) (2015).
37. Sun, J., Chen, Q., Zhang, Y. & Zuo, C. Efficient positional misalignment correction method for fourier ptychographic microscopy. *Biomedical Optics Express* **7**, 1336–1350, doi:[10.1364/BOE.7.001336](https://doi.org/10.1364/BOE.7.001336) (2016).
38. Sun, J., Chen, Q., Zhang, Y. & Zuo, C. Sampling criteria for fourier ptychographic microscopy in object space and frequency space. *Optics Express* **24**, 15765–15781, doi:[10.1364/OE.24.015765](https://doi.org/10.1364/OE.24.015765) (2016).
39. Zuo, C., Sun, J. & Chen, Q. Adaptive step-size strategy for noise-robust fourier ptychographic microscopy. *Optics Express* **24**, 20724–20744, doi:[10.1364/OE.24.020724](https://doi.org/10.1364/OE.24.020724) (2016).
40. Fischer, A. H., Jacobson, K. A., Rose, J. & Zeller, R. Hematoxylin and eosin staining of tissue and cell sections. *Cold Spring Harbor Protocols* **2008**, pdb–prot4986, doi:[10.1101/pdb.prot4986](https://doi.org/10.1101/pdb.prot4986) (2008).
41. Greenbaum, A. *et al.* Increased space-bandwidth product in pixel super-resolved lensfree on-chip microscopy. *Scientific reports* **3**, doi:[10.1038/srep01717](https://doi.org/10.1038/srep01717) (2013).
42. Luo, W., Greenbaum, A., Zhang, Y. & Ozcan, A. Synthetic aperture-based on-chip microscopy. *Light: Science & Applications* **4**, e261 (2015).

## Acknowledgements

This work was financially supported by National Natural Science Fund of China (11574152, 61505081), ‘Six Talent Peaks’ project (2015-DZXX-009, Jiangsu Province, China) and ‘333 Engineering’ research project (BRA2015294, Jiangsu Province, China), Fundamental Research Funds for the Central Universities (30915011318, 30916011322), and Open Research Fund of Jiangsu Key Laboratory of Spectral Imaging & Intelligent Sense (3092014012200417). C. Zuo thanks the support of the ‘Zijin Star’ program of Nanjing University of Science and Technology.

## Author Contributions

J.S. and C.Z. conceived and designed the experiments. J.S. and L.Z. built the experimental platform. J.S. performed the experiments and processed the resulting data. J.S. and C.Z. analysed the results and wrote the manuscript. C.Z. and Q.C. supervised the project. All the authors contributed to discussion on the results for this manuscript.

## Additional Information

**Supplementary information** accompanies this paper at doi:[10.1038/s41598-017-01346-7](https://doi.org/10.1038/s41598-017-01346-7)

**Competing Interests:** The authors declare that they have no competing interests.

**Publisher's note:** Springer Nature remains neutral with regard to jurisdictional claims in published maps and institutional affiliations.



**Open Access** This article is licensed under a Creative Commons Attribution 4.0 International License, which permits use, sharing, adaptation, distribution and reproduction in any medium or format, as long as you give appropriate credit to the original author(s) and the source, provide a link to the Creative Commons license, and indicate if changes were made. The images or other third party material in this article are included in the article's Creative Commons license, unless indicated otherwise in a credit line to the material. If material is not included in the article's Creative Commons license and your intended use is not permitted by statutory regulation or exceeds the permitted use, you will need to obtain permission directly from the copyright holder. To view a copy of this license, visit <http://creativecommons.org/licenses/by/4.0/>.

© The Author(s) 2017